Robotica (2022), **40**, pp. 2651–2665
doi:10.1017/S0263574721001867

CAMBRIDGE
UNIVERSITY PRESS

RESEARCH ARTICLE

An obstacle-avoiding and stiffness-tunable modular bionic soft robot

Zhaoyu Liu, Yuxuan Wang, Jiangbei Wang, Yanqiong Fei* and Qitong Du

Research Institute of Robotics, Shanghai Jiaotong University, Shanghai 200240, China
*Corresponding author. E-mail: fyq_sjtu@163.com

Received: 17 September 2021; **Revised:** 16 November 2021; **Accepted:** 1 December 2021;
First published online: 6 January 2022

Keywords: soft robot, modular robot, nonlinear variable stiffness, obstacle-avoiding ability

Abstract

The aim of this work is to design and model a novel modular bionic soft robot for crawling and crossing obstacles. The modular bionic soft robot is composed of several serial driving soft modules, each module is composed of two parallel soft actuators. By analyzing the influence of working pressure and manufacturing size on the stiffness of the modular bionic soft robot, the nonlinear variable stiffness model of the modular bionic soft robot is established. Based on this model, the spatial states and design parameters of the modular bionic soft robot are discussed when the modular bionic soft robot can pass through the obstacle. Experiments show that when the inflation air pressure of the modular bionic soft robot is 70 kPa, its speed can reach 7.89 mm/s and the height of obstacles passed by it can reach 42.8 mm. The feasibility of the proposed modular bionic soft robot and nonlinear variable stiffness model is verified by locomotion experiments.

1. Introduction

Soft robots are made of flexible materials, which can arbitrarily change their shapes and sizes in a wide range. They have infinite degrees of freedom so that theirs end effector can reach any point in the workspace in theory [1]. Soft robots have excellent environmental adaptability and flexibility which allow them to pass through obstacles by passive deforming and move forward in different shapes by active deforming. They can imitate the locomotion pattern of animals to reach the harsh environment to expand the field of human exploration. Because of the above advantages, they have broad applications in the fields of reconnaissance, detection, rescue and medical treatment.

In recent studies, various soft robots have been developed [2–5]. Most soft robots are inspired by natural creatures, including creeping (earthworm-like) [6], crawling (inchworm-like) [7], multi-legged (dog-like) [8] and swimming (fish-like) [9]. Kim et al. develop a bionic turtle-like robot with an intelligent soft combination structure [10]. Hubbard et al. apply ionic polymer-metal composite (IPMC) to biomimetic swimming robotic fish to drive its pectoral and caudal fins [11]. Nakamaru et al. develop a bionic robot with the inchworm-like locomotion pattern using the gel as material [12]. The robot uses the driving characteristic of the B-Z chemical reaction to move through self-oscillation. Pang et al. develop a modular soft robot which is composed of four deformable silicone rubber units [13]. It can crawl through the transformation between different modules.

The soft crawling robot is an important part of soft robots, which can be applied to complex and changeable terrain [14]. In nature, most creatures can store elastic potential energy through their soft muscles and skins [15]. In this way, soft crawling robots can better adapt to different environments. Shepherd et al. develop an inflatable peristaltic soft robot that can turn and crawl by changing the rhythm of different parts of the body [16]. Wang et al. design a shape memory alloy (SMA)-driven soft robot inspired by inchworms. The robot has a novel structure and consists of three functional components. It can achieve bidirectional linear and rotational locomotion [17].

© The Author(s), 2022. Published by Cambridge University Press.

https://doi.org/10.1017/S0263574721001867 Published online by Cambridge University Press

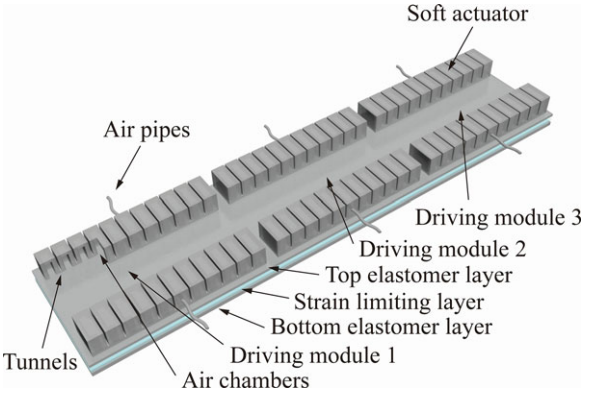


Figure 1. *The spatial view of the modular bionic soft robot.*

In the locomotion process of soft crawling robots, sometimes they need to pass through some narrow channels. For rigid crawling robots, they can avoid obstacles by changing their shapes [18–20]. For the soft crawling robots, it is a good idea to change the stiffness of their own structures to avoid obstacles [21]. At present, the research on the variable stiffness of soft robots is mainly focused on soft grippers [22–28]. The stiffness of the gripper is controlled by adding the variable stiffness control layer to improve the grasping ability. Li et al. design a gripper based on a novel passive particle interference principle [29]. When the pressure changes from 20 kPa to 80 kPa, the stiffness can be increased more than sixfold. However, the concept of variable stiffness is rarely mentioned in the research of soft crawling robots. This paper proposes a method to combine the soft crawling robot with variable stiffness technology to realize the obstacle avoidance locomotion of the soft crawling robot.

In this study, a novel modular bionic soft robot is designed, which consists of three driving modules in series. Unlike previous soft crawling robots, the proposed modular bionic soft robot uses a modular design to improve the speed and controllability of the robot. A stiffness-tunable model of the modular bionic soft robot is established with mechanical analysis. By changing the working pressure and manufacturing size of the modular bionic soft robot, the robot has the best stiffness.

2. Design and modeling

This section introduces the parameter selection and structure of the soft actuator of the modular bionic soft robot. The analysis of the nonlinear deformation characteristics of the soft actuator is also introduced.

2.1. Design of soft actuators

The main body of the modular bionic soft robot in Fig. 1 is made of silicone rubber. The whole robot consists of three driving modules, each of which is divided into four parts: two soft actuators juxtaposed above, a top elastomer layer, a bottom elastomer layer and the strain limiting layer located in the middle [30]. One soft actuator has 11 air chambers and each of them is connected by a tunnel located at the bottom of the air chambers (Fig. 1). Each driving module has two air pipes, each of which is inserted into the middle air chamber of the actuator. During inflation, the air passing through the inflatable pipe reaches the middle air chamber of the soft actuator and then reaches each air chamber through the tunnel. With the increase of air chamber pressure, each air chamber expands to drive the driving module to bend. As shown in Fig. 2(b), the partition walls of chambers bulge to contact each other after inflation. The manufacturing parameters of the air chamber are shown in Fig. 2(a) and (c) and their values are shown in Table I. They are determined by model and experience. The establishment of the model is described in Section 2.2.

https://doi.org/10.1017/S0263574721001867 Published online by Cambridge University Press

Table I. *Manufacturing parameters of soft actuators.*

Parameters	Values
a	12 mm
b	20 mm
c	2 mm
d	2.5 mm
e	2 mm
f	4 mm
k	1 mm
m	2 mm
n	3 mm

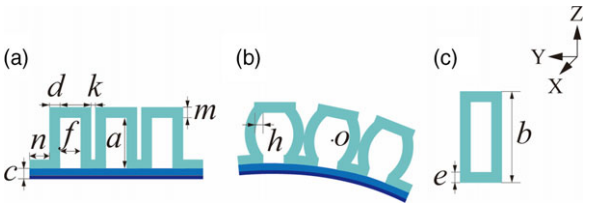


Figure 2. *Sectional view of air chambers. (a) Before inflating view and (b) after inflating view. (c) Top sectional view.*

The nonlinear deformation process of each soft actuator can be divided into four stages: (1) driving module 1 inflates. In the initial process, since module 2 and module 3 of the modular bionic soft robot are flat on the ground, the friction between the front and the rear of module 1 and the ground is different, so the rear of the modular bionic soft robot is rolled forward after module 1 is inflated. (2) Driving module 1 deflates while driving module 2 inflates. During the deflation of driving module 1, due to the deformation and bending of the modular bionic soft robot after inflation, the rear of the modular bionic soft robot is in inclined contact with the ground, resulting in large rear end friction, which makes the modular bionic soft robot extend forward during the deflation process. When driving module 2 is inflated at the same time, the rear end of driving module 2 will stretch driving module 1 forward. (3) Driving module 3 inflates while driving module 2 deflates. The process is similar to stage 2. (4) Driving module 3 deflates. Since driving module 1 and driving module 2 of the modular bionic soft robot are flat on the ground, the friction between the front and the rear of driving module 3 and the ground is different, so the front of the modular bionic soft robot extends forward when driving module 3 deflates.

During the locomotion of the modular bionic soft robot, the bottom friction of the modular bionic soft robot is different when different modules inflate and deform. As shown in Fig. 3, the distance of the robot moving forward in a modular bionic soft is S through the cyclic inflating and deflating behavior of module 1, module 2 and module 3.

2.2. Analysis of nonlinear deformation characteristics

The nonlinear deformation analysis of the soft actuator is carried out to determine the variation of displacement h of the expansion wall of the air chamber with the inflation pressure P. As shown in Fig. 2(a) and (c), the cavity in the exhausted state is rectangular with a gap k. When inflated, the partition walls of the air chamber expand and contact each other, as shown in Fig. 2(b). We assume that the partition wall expands into a cylindrical surface (i.e., an arc on the sectional view) and contacts each other in a tangent manner. Compared with the contact wall, the deformation of the thicker top and side walls is much smaller, so it is assumed that the chamber height b is constant during expansion. In addition, when the

https://doi.org/10.1017/S0263574721001867 Published online by Cambridge University Press

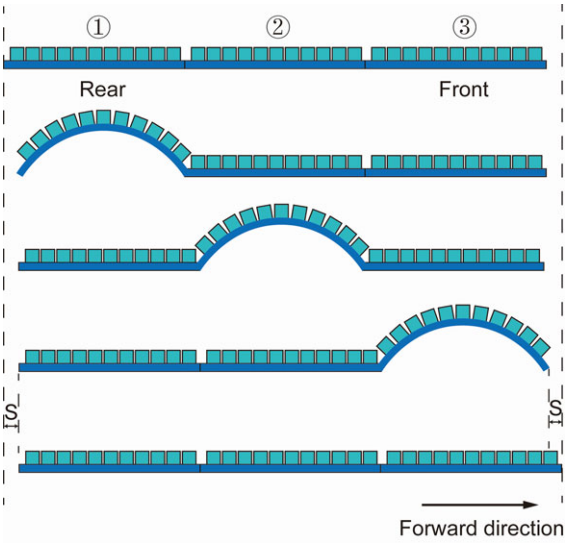


Figure 3. *Locomotion process of the modular bionic soft robot in one period.*

expansion is extruded by an external force, the top and side walls will protrude. Through experiments, we have observed that the convexity of the top and side walls is much smaller than that of the contact walls. In this study, in order to simplify the model, only the deformation of the contact wall is considered, and the deformation is h. Assuming that the silicone rubber material is incompressible ($I_3 = 1$) and isotropic, the deformation of silicone rubber can be analyzed by strain energy density function [31].

$$W = W(I_1, I_2, I_3) \tag{1}$$

where W is the strain energy density, and I_1, I_2 and I_3 are the three invariants of the deformation tensor.

$$\begin{cases} I_1 = \lambda_1^2 + \lambda_2^2 + \lambda_3^2 \\ I_2 = \lambda_1^{-2} + \lambda_2^{-2} + \lambda_3^{-2} \\ I_3 = \lambda_1^2 \lambda_2^2 \lambda_3^2 = 1 \end{cases} \tag{2}$$

Among Eq. (2), λ_i is the main elongation ratio in three directions.

According to the relationship between stress and strain of silicone rubber material, the relationship between principal stress and principal elongation ratio of silicone rubber material can be obtained:

$$\sigma_1 = \frac{2}{\lambda_1}\left(\lambda_1{}^2 - \frac{1}{\lambda_1^2\lambda_2^2}\right)\left(\frac{\partial W}{\partial I_1} + \lambda_2^2\frac{\partial W}{\partial I_2}\right) \tag{3}$$

$$\sigma_2 = \frac{2}{\lambda_2}\left(\lambda_2{}^2 - \frac{1}{\lambda_1^2\lambda_2^2}\right)\left(\frac{\partial W}{\partial I_1} + \lambda_1^2\frac{\partial W}{\partial I_2}\right) \tag{4}$$

Among Eqs. (3) and (4), σ_1, σ_2 are the principal stresses in both directions of the tensile plane.

With Yeoh model, the binomial parameter form [32] of the strain energy function is

$$W = C_1(I_1 - 3) + C_2(I_2 - 3)^2 \tag{5}$$

Among Eq. (6), $C_1, C_2$are material coefficients, which are determined by tensile tests (BYES, 5000 N, 700 mm, China). According to the standard ASTMD412 and then curve fitting, which results in $C_1 = 0.112$ and $C_2 = 0.019$. o is located at the center of a single air chamber as the coordinate origin, and Y direction is the expansion direction of the air chamber wall. In the process of inflation, any point on the air chamber wall moves in the Y direction, while the X and Z coordinates remain unchanged

https://doi.org/10.1017/S0263574721001867 Published online by Cambridge University Press

(Fig. 2(b)). The displacement of any point on the left air chamber wall is U, as shown in Eq. (8). By integrating the left air chamber wall, the corresponding strain energy function is obtained, as shown in Eqs. (4) and (5).

$$E = \int Wdv = \int_{\frac{c}{2}}^{\frac{c}{2}+d} \int_{-\frac{b}{2}}^{\frac{b}{2}} \int_{-\frac{a}{2}}^{\frac{a}{2}} C_1(I_1 - 3) + C_2(I_2 - 3)^2 \, dxdzdy \tag{6}$$

$$I_1 = tr\left[\left(I + \frac{\partial(U)}{\partial(x, y, z)}\right)\left(I + \frac{\partial(U)}{\partial(x, y, z)}\right)^T\right] \tag{7}$$

$$U = (U_x, U_y, U_z) = \left(0, hf\left(\frac{2z}{a}\right) f\left(\frac{2x}{b}\right)\right) \tag{8}$$

where v is the volume of a single left air chamber wall, I is a unit matrix and $f(\tau)$ is called the profile function. a,b,c and d are manufacturing parameters of the air chamber (Fig. 2). According to Eqs. (6)–(8), strain energy can be obtained.

$$E = 4C_2\left[A_0A_1\left(\frac{a^2}{b^2} + \frac{b^2}{a^2}\right) + 2C^2\right]\frac{h^4d}{ab} + 4C_1B_0B_1\left(\frac{a}{b} + \frac{b}{a}\right)h^2d \tag{9}$$

Among Eq. (9),$A_0, A_1, B_0, B_1, C$are constants, which are determined by function $f(\tau)$:

$$\begin{cases} A_0 = \int_0^1 [f(\tau)]^4 d\tau \\ A_1 = \int_0^1 [f'(\tau)]^4 d\tau \\ B_0 = \int_0^1 [f(\tau)]^2 d\tau \\ B_1 = \int_0^1 [f'(\tau)]^2 d\tau \\ C = \int_0^1 [f(\tau)]^2 [f'(\tau)]^2 d\tau \end{cases} \tag{10}$$

Generally, $f(\tau)$ should comply with the actual deformation of the left air chamber wall as following conditions, $f(0) = 1$, $f(-1) = f(1) = 0$, $f'(0) = 0$.

To simplify the function, we construct the function $f(\tau) = 1 - \tau^2$. Then, the constants are calculated according to $f(\tau)$.

By using the principle of virtual work, the expansion pressure P is connected with the maximum displacement h, and Eq. (11) is obtained. The left side is the virtual change of the total strain energy of the left air chamber wall with the expansion height, and the right side is the virtual work of the left air chamber wall under the expansion pressure.

$$\frac{dE(h)}{dh}\delta h = P\frac{dV(h)}{dh}\delta h \tag{11}$$

$$V(h) = hab\int_0^1 [f(\tau)]^2 d\tau \tag{12}$$

Among Eq. (12), V(h) is the increased volume inside the air chamber after inflating. Among Eqs. (9)–(12), the relationship between the pressure P inside the air chamber and the maximum displacement h of the air chamber expansion wall can be obtained.

$$P = \left[0.2340\left(\frac{a^2}{b^2} + \frac{b^2}{a^2}\right) + 0.0334\right]\frac{h^3d}{a^2b^2} \tag{13}$$

According to Eq. (10), the pressure P is proportional to the cubic of the deformation h of the air chamber expansion wall. With the increase of the pressure in the air chamber, the expansion speed of the air chamber slows down. The manufacturing parameters of the air chamber are shown in Table I. Parameters a, b and d are obtained from Eq. (13). Other parameters have little influence on the deformation of

https://doi.org/10.1017/S0263574721001867 Published online by Cambridge University Press

the air chamber during inflation. Therefore, other parameters are determined by the manufacturing requirements.

When the pressure P increases, the deformation of the air chamber increases. The bending angle of the driving module will also increase. However, in the inflation experiment, when the pressure P exceeds 90 kPa, the structure of the driving module will be damaged. Considering the characteristics of silicone rubber and the safety of the driving module, the air pressure of the driving module is set at 70 kPa.

3. Stiffness-tunable control

In the process of the modular bionic soft robot moving forward, the expansion and deformation height of each driving module directly determine the maximum height of the modular bionic soft robot passing through the narrow terrain. At the same time, the deformation height indirectly affects the motion speed and vibration amplitude of the modular bionic soft robot, so it is necessary to study the factors affecting the deformation height of the driving module in the process of inflation and deflation. In the locomotion process, we divide the robot's modules into the main motion module and the auxiliary motion module. The main motion module is used to generate the overall motion of the robot, and the auxiliary motion module is used to change the stiffness, space state and motion speed of the robot. For the modular bionic soft robot, on the one hand, the deformation height of the driving module is determined by the manufacturing sizes and materials of the modular bionic soft robot, and on the other hand, it is determined by the inflation pressure P of the main motion module and the inflation pressure P_0 of the auxiliary motion module. For the auxiliary motion module, the stiffness changes with the change of inflation air pressure. In a certain range of air pressure, the stiffness of the modular bionic soft robot increases with the increase of air pressure of the auxiliary motion module. By adjusting the pressure of the auxiliary motion module, the height of the modular bionic soft robot can be controlled, and the modular bionic soft robot can pass through some lower obstacles.

In order to study the change of the overall height of the modular bionic soft robot when the stiffness of the auxiliary motion module changes, the motions of the modular bionic soft robot are classified into Type A and Type B. Type A: module 2 is the main motion module. Type B: module 1 or module 3 is the main motion module.

3.1. Type A: module 2 is the main motion module

When module 2 is the main motion module, the modular bionic soft robot model is shown in Fig. 4, then the overall motion height of the modular bionic soft robot is $H = h_0 + h_1 + h_2$.

It is easy to get h_0 from the manufacturing parameters of a single driving module. The bending angle ϕ of module 2 can be obtained in Eq. (14). Equation (14) shows that the bending angle ϕ is related to the inflation pressure P of module 2.

$$\varphi = \frac{2(N-1)\left\{\sqrt[3]{\frac{Pa^2b^2}{d\left[0.234\left(\frac{a^2}{b^2}+\frac{b^2}{a^2}\right)+0.0334\right]}}-\frac{k}{2}\right\}}{\frac{a}{2}+c} \tag{14}$$

As shown in Fig. 4(a), L is the original length of the main motion module, R is the radius of curvature when the structure is bent and ϕ is the central angle after deformation.

$$L = (f + 2d)N + (N-1)k + 2n = R\varphi \tag{15}$$

$$h_1 = R - R\cos\frac{\varphi}{2} \tag{16}$$

https://doi.org/10.1017/S0263574721001867 Published online by Cambridge University Press

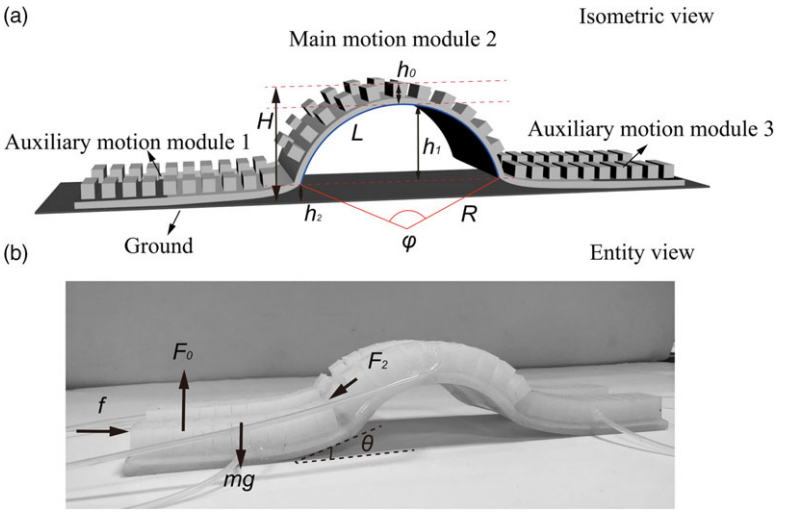


Figure 4. *Module 2 is the main motion module, (a) the model of the modular bionic soft robot and (b) the actual modular bionic soft robot.*

After obtaining h_1, the force analysis of the auxiliary motion module 1 is carried out, as shown in Fig. 4(b). f is the frictional force on the auxiliary motion module 1. F_0 is the ground support force of the auxiliary motion module 1. F_2 is the force exerted by the main motion module on the auxiliary motion module 1.

$$F_2 \sin\theta + mg = F_0 \tag{17}$$

$$F_2 \cos\theta = \mu F_0 \tag{18}$$

After the lifting angle θ of auxiliary motion module 1 is obtained, it is necessary to determine the lifting height when auxiliary motion module 1 is not inflated. At the beginning of the movement, the inflation pressure of module 2 increases, the bending angle ϕ of module 2 increases with the increase of inflation pressure P, and the lifting angle θ of auxiliary motion module 1 increases from 0°. As shown in Fig. 5(a), the lifting height h of auxiliary motion module 1 is a piecewise function $f(\theta)$ which varies with the lifting angle of auxiliary motion module 1, and the expression of $f(\theta)$ is as follows:

$$f(\theta)_1 = k \sin\frac{\theta}{2} + (2d + f + n)\sin\theta,\ 0 \le \theta \le \pi - 2\cos^{-1}\frac{k}{2a} \tag{19}$$

$$\begin{aligned} f(\theta)_2 = {} & k\left[\sin\left(\theta - \frac{\pi}{2} + \cos^{-1}\frac{k}{2a}\right) + \sin\left(\frac{\theta}{2} - \frac{\pi}{2} + \cos^{-1}\frac{k}{2a}\right)\right] + (2d + f + n)\sin\theta \\ & + (2d + f)\sin\left(\theta - \pi + 2\cos^{-1}\frac{k}{2a}\right), \quad \pi - 2\cos^{-1}\frac{k}{2a} \le \theta \le 2\left(\pi - 2\cos^{-1}\frac{k}{2a}\right) \end{aligned} \tag{20}$$

$$\begin{aligned} f(\theta)_3 = {} & k\left[\sin\left(\theta - \frac{\pi}{2} + \cos^{-1}\frac{k}{2a}\right) + \sin\left(\theta - \frac{3\pi}{2} + 3\cos^{-1}\frac{k}{2a}\right) + \sin\left(\frac{\theta}{2} - \pi + 2\cos^{-1}\frac{k}{2a}\right)\right] \\ & + (2d + f + n)\sin\theta + (2d + f)\left[\sin\left(\theta - \pi + 2\cos^{-1}\frac{k}{2a}\right)\right. \\ & \left. + \sin\left(\theta - 2\pi + 4\cos^{-1}\frac{k}{2a}\right)\right], 2\left(\pi - 2\cos^{-1}\frac{k}{2a}\right) \le \theta \le 3\left(\pi - 2\cos^{-1}\frac{k}{2a}\right) \end{aligned} \tag{21}$$

https://doi.org/10.1017/S0263574721001867 Published online by Cambridge University Press

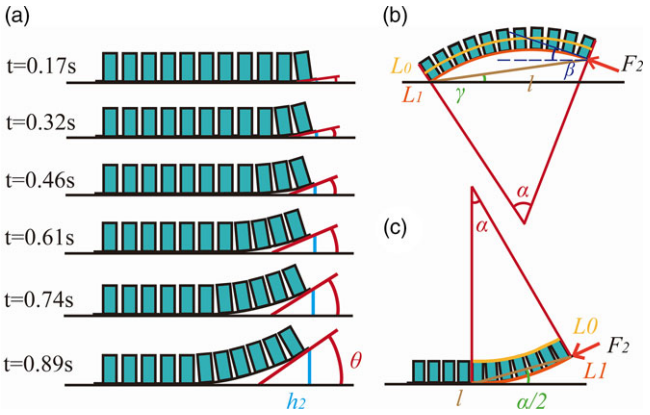


Figure 5. *(a) When the modular bionic soft robot moves, the displacement of the auxiliary motion module 1 changes with time, (b) when module 2 is the main motion module, the force analysis diagram of module 1 during inflation, (c) when module 2 is the main motion module, the force analysis diagram of auxiliary motion module 1.*

$$f(\theta)_4 = k\left[\sin\left(\theta - \frac{\pi}{2} + \cos^{-1}\frac{k}{2a}\right) + \sin\left(\theta - \frac{3\pi}{2} + 3\cos^{-1}\frac{k}{2a}\right) + \sin\left(\theta - \frac{5\pi}{2} + 5\cos^{-1}\frac{k}{2a}\right) + \sin\left(\frac{\theta}{2} - \frac{3\pi}{2} + 3\cos^{-1}\frac{k}{2a}\right)\right] + (2d + f + n)\sin\theta + (2d + f)\left[\sin\left(\theta - \pi + 2\cos^{-1}\frac{k}{2a}\right) + \sin\left(\theta - 2\pi + 4\cos^{-1}\frac{k}{2a}\right) + \sin\left(\theta - 3\pi + 6\cos^{-1}\frac{k}{2a}\right)\right], 3\left(\pi - 2\cos^{-1}\frac{k}{2a}\right) \le \theta \le 4\left(\pi - 2\cos^{-1}\frac{k}{2a}\right) \tag{22}$$

Through Eqs. (19)–(22), the deformed height of the actuator in other states can be deduced. After getting the elevation height of auxiliary motion module 1 in the initial state, the change of h_2 is analyzed when its stiffness changes (i.e., driving module 1 inflates). When the expansion wall displacement $h \le k/2$, driving module 1 bends downward. When the expansion wall displacement $h > k/2$, driving module 1 expands upward.

(1) Expansion wall displacement $h \le k/2$.
When the inflation pressure of module 2 is 70 kPa, module 1 is lifted by six chambers in the initial state, and the geometric analysis is carried out, as shown in Fig. 5(c).

$$\begin{cases} L_0 = 7(2d + f) + 12h = (R + m + 12h)\alpha \\ L_1 = 7(2d + f) + 6k = (R + c + m + a)\alpha \end{cases} \tag{23}$$

It can be solved:

$$\alpha = \frac{6(k - 2h)}{c + a - 12h} \tag{24}$$

So we can get the height h2,

$$h_2 = l\sin\frac{\alpha}{2} \tag{25}$$

(2) Expansion wall displacement $h > k/2$.

https://doi.org/10.1017/S0263574721001867 Published online by Cambridge University Press

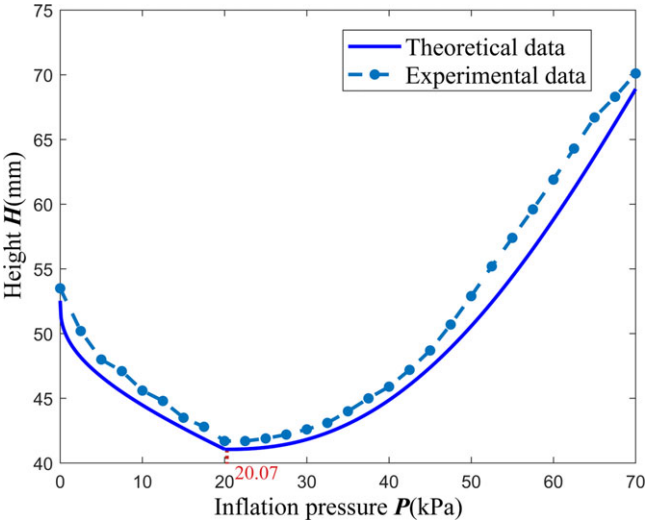


Figure 6. *Relationship between inflation pressure P of the modular bionic soft robot and the whole height H of the modular bionic soft robot.*

The inflation pressure of module 2 is 70 kPa. Module 1 begins to expand and bend, and the geometric analysis is carried out, as shown in Fig. 5 (b).

$$\begin{cases} L_1 = 11(2d+f) + 10k = R\alpha \\ L_0 = 11(2d+f) + 20h = (R + c + \dfrac{a}{2})\alpha \end{cases} \tag{26}$$

It can be solved:

$$\alpha = \frac{10(2h-k)}{c + \dfrac{a}{2}} \tag{27}$$

It can be obtained from geometric relations.

$$\gamma = \frac{\alpha}{2} - \beta \tag{28}$$

$$h_2 = l \sin \gamma \tag{29}$$

Therefore, by combining h, the relationship curves between the overall height H of the modular bionic soft robot and the inflation pressure P of the module 1 and module 3 can be obtained.

The curves in Fig. 6 show that when the inflation pressure P of module 1 and module 3 is less than 20.07 kPa, the stiffness of module 1 and module 3 increases, the bending of module 1 and module 3 decreases and the overall height H of module decreases. When the inflation pressure of module 1 and module 3 is greater than 20.07 kPa, the stiffness of module 1 and module 3 continues to increase, resulting in obvious expansion deformation, which makes the overall height H of the module increase rapidly. Therefore, when the inflation pressure of module 1 and module 3 equals 20.07 kPa, the overall height of the modular bionic soft robot is the lowest, and the height of the narrow terrain through which it can pass is the lowest. At this time, the stiffness of module 1 and module 3 is the best.

By comparing the experimental data, as shown in Fig. 6, the solid line is the theoretical curve and the dotted line is the experimental acquisition curve. By comparing the experimental data with the theoretical data, the error is found, and the error is relatively stable. The main reason is that the thickness of the bottom plate of the modular bionic soft robot is slightly thicker than that of the design, which makes the overall height of the actual module slightly higher than that of the theoretical data.

https://doi.org/10.1017/S0263574721001867 Published online by Cambridge University Press

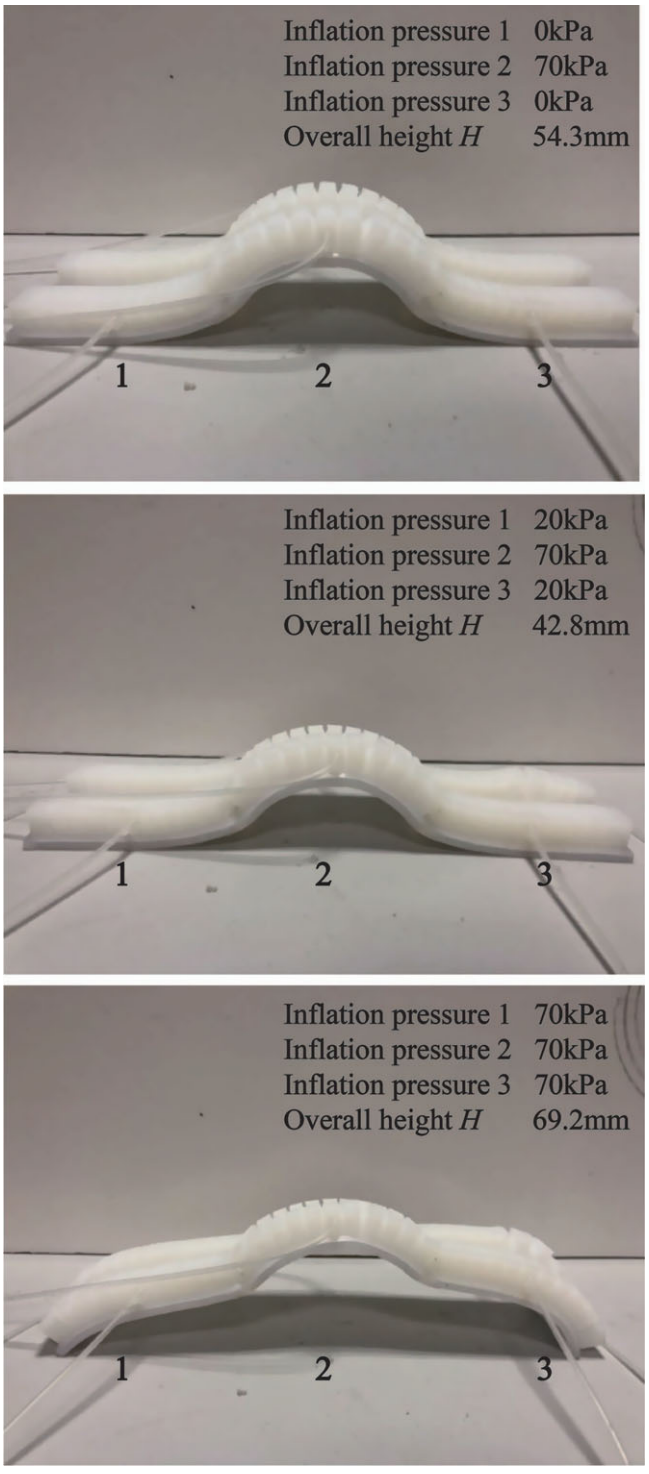


Figure 7. *Schematic diagram of height change of the modular bionic soft robot.*

https://doi.org/10.1017/S0263574721001867 Published online by Cambridge University Press

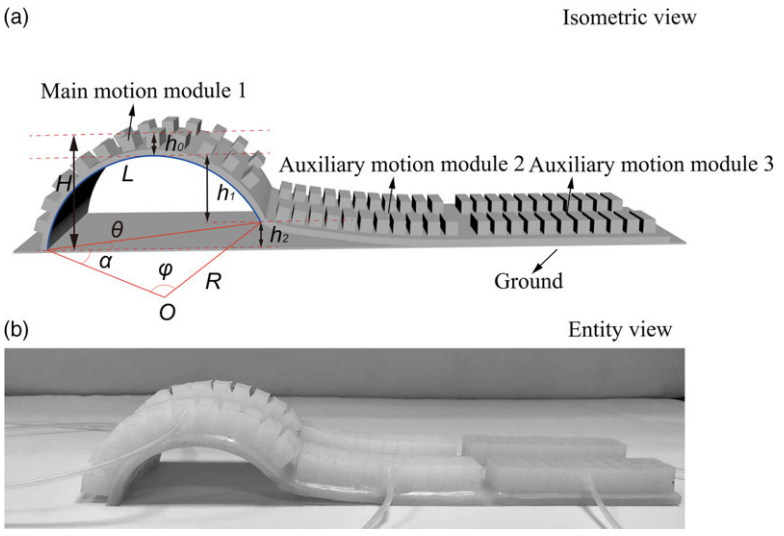


Figure 8. *When module 1 or module 3 is the main motion module, (a) the model of the modular bionic soft robot and (b) the actual modular bionic soft robot.*

As shown in Fig. 7, with the inflation pressure of module 2 unchanged, the inflation pressure of module 1 and module 3 increases, which changes the stiffness of the module. The overall height of the modular bionic soft robot first decreases and then increases. When the inflation pressure is 20 kPa, the overall height of the modular bionic soft robot is the lowest, and the height of the narrow terrain through which it could pass is the lowest. This height is 42.8 mm.

3.2. Type B. Module 1 or module 3 is the main motion module.

At this time, the model of the modular bionic soft robot is shown in Fig. 8, and the overall height of the modular bionic soft robot is $H = h_0 + h_1$.

Module 1 needs to be analyzed when calculating h_1, as shown in Fig. 8(a). Assuming that the center of the circle corresponding to module 1 is O, and the distance between the center of the circle and the highest point of module 1 is R, the vertical distance between the point O and the ground can calculate the overall height of the three modules.

$$\theta = \sin^{-1}\left[\frac{h_2}{2R\sin\left(\frac{\varphi}{2}\right)}\right] \tag{30}$$

$$\alpha = \frac{\pi}{2} - \frac{\varphi}{2} - \theta \tag{31}$$

$$y_0 = R\sin\varphi \tag{32}$$

$$h_1 = R - y_0 \tag{33}$$

Comparing the data of type B with the data of type A, it can be found that under the same conditions, the overall height of the modular bionic soft robot is higher when module 2 is the main motion module, which is the highest height that the modular bionic soft robot can pass through obstacles.

After adjusting the stiffness of different modules, it can be observed in the experiment that the motion height of the modular bionic soft robot decreases, the vibration amplitude decreases and the motion speed increases. The optimum stiffness of the auxiliary motion module will also change under different

https://doi.org/10.1017/S0263574721001867 Published online by Cambridge University Press

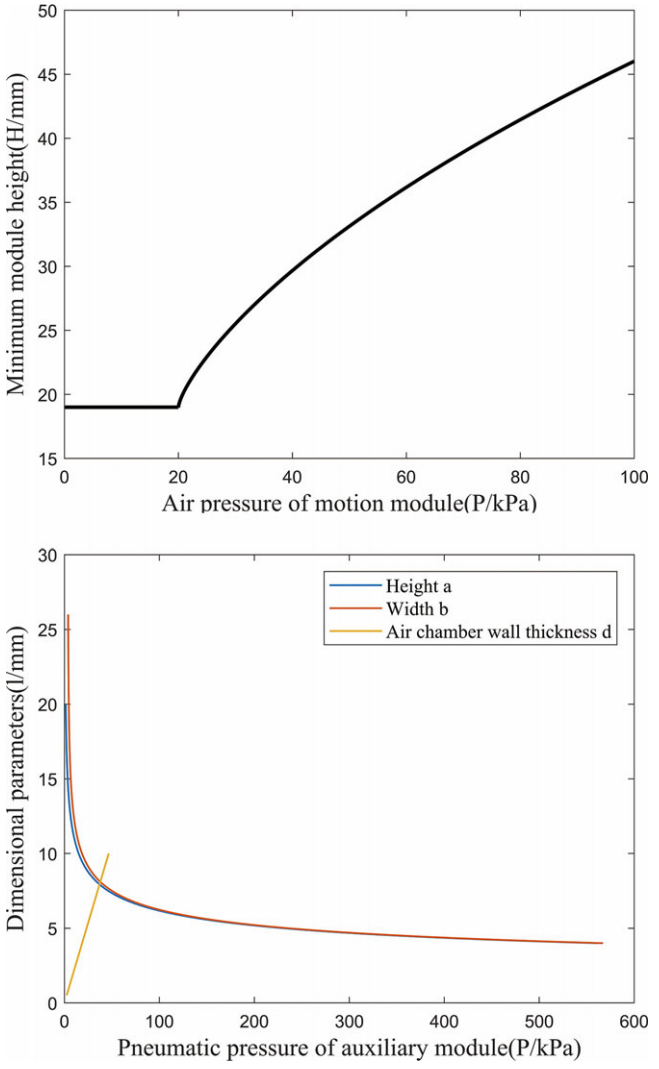


Figure 9. *(a) The relationship between the main motion module P and the minimum height H of the modular bionic soft robot (b) the relationship between the module size a, b, d and the inflation pressure P of the auxiliary motion module.*

air pressure of the main motion module. The optimum air pressure of the deflation module can be calculated by Eqs. (25) and (29).

When the manufacturing size of the module remains unchanged, the minimum height H of the modular bionic soft robot varies with the change of the pressure of the main motion module P, as shown in Fig. 9(a). The relationship between module dimensions a, b, d and inflation pressure P of deflation module is shown in Fig. 9(b).

4. Obstacle avoidance experiment

For the modular bionic soft robot, through theoretical analysis, it can be found that when the air pressure of the auxiliary motion module is about 20 kPa, the modular bionic soft robot can pass through the narrow terrain with the lowest height. The modular bionic soft robot is tested on the experimental platform.

https://doi.org/10.1017/S0263574721001867 Published online by Cambridge University Press

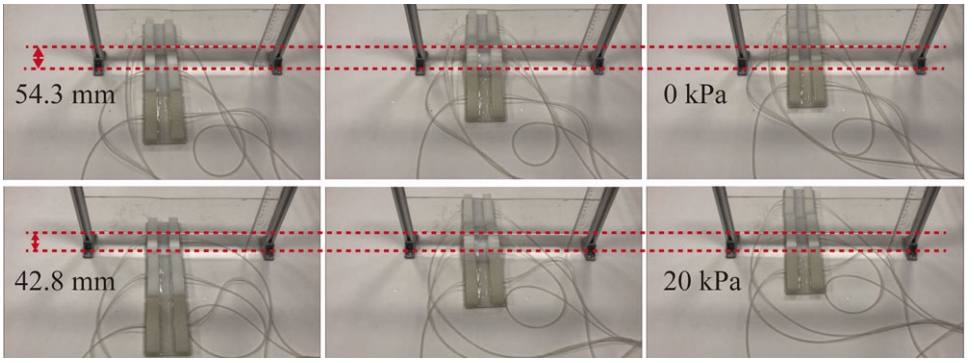


Figure 10. *When the air pressure of the main motion module is 70 kPa and that of the auxiliary motion module is 0 kPa and 20 kPa, respectively, the height of the modular bionic soft robot passing through the obstacle.*

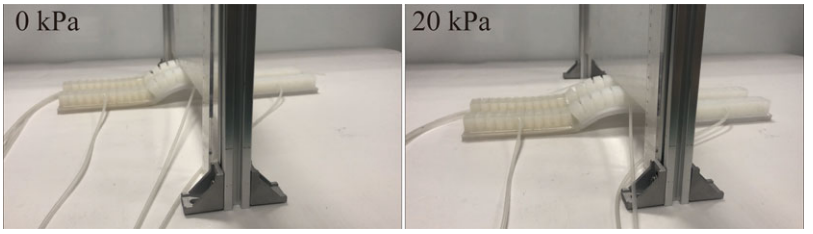


Figure 11. *Side view of the height of the modular bionic soft robot passing.*

The height of the modular bionic soft robot passing through the obstacle was compared when the air pressure of the main motion module is 70 kPa and the air pressure of the auxiliary motion module is 0 and 20 kPa. As shown in Fig. 10, it is found that the height of obstacles passed by the modular bionic soft robot at 20 kPa is nearly 13 mm lower than that of obstacles passed by the modular bionic soft robot at 0 kPa. Through the experiment, it is found that the speed of the modular bionic soft robot can reach 7.89 mm/s during the locomotion. Therefore, it can be explained that under the appropriate air pressure, the modular bionic soft robot can more effectively complete the obstacle avoidance function.

As shown in Fig. 11, by comparing the side view (0 kPa on the left and 20 kPa on the right), it can be found that the modular bionic soft robot adjusted by variable stiffness will not collide with the obstacle obviously when it passes through the obstacle at the same height. In the actual working process, the modular bionic soft robot should have the ability to pass through obstacles without touching obstacles to adapt to the uncertainty of its working environment.

5. Conclusion

In this paper, a modular bionic soft robot with variable stiffness is constructed. It consists of three driving modules in series, each of which consists of two parallel air chambers and a bottom plate. The nonlinear locomotion pattern and variable stiffness model of the robot are given by mechanical analysis in this paper. By controlling the stiffness of the actuator with different pressure, the height of the modular bionic soft robot is controlled during the motion. Thus, the modular bionic soft robot can adapt to different working environments and pass through different heights obstacles most efficiently. Experiments are carried out to verify the effect of the robot passing through obstacles in the initial state (the pressure of the auxiliary module is 0 kPa) and the stiffness change state (the pressure of the auxiliary module is 20 kPa). According to the experiment, the height of obstacles passed by the soft robot in the initial state is

https://doi.org/10.1017/S0263574721001867 Published online by Cambridge University Press

54.3 mm, and the height of obstacles passed by the soft robot in the changing stiffness state is 42.8 mm. The speed of the modular bionic soft robot can reach 7.89 mm/s.

By controlling the stiffness of the robot, it can better accomplish the task of crossing obstacles. Because of the flexible structure of the robot, it can also be applied to complex and changeable environments. This kind of robot can also be used in earthquake rescue and reconnaissance missions that humans or rigid robots cannot access. Future work will focus on the integration of this kind of soft robot and its application in different environments.

Acknowledgements. This work was supported by Institute of Medical Robotics of Shanghai Jiao Tong University under Grant No. IMR2019KY01, National Natural Science Foundation of China under Grant No. 51875335, Project No. 2021Szvup078, TMSK-2021-110.

Authors' Contributions. Zhaoyu Liu designed and manufactured a modular differential drive robot, and completed the modeling and experimental part. Yuxuan Wang contributed significantly to analysis and manuscript preparation. Jiangbei Wang performed the data analyses. Yanqiong Fei helped perform the analysis with constructive discussions. Qitong Du participated in the revision of the manuscript.

Conflict of Interest. The authors declare that they have no conflict of interest.

References

[1] A. Crespi and A. J. Ijspeert, "AmphiBot II: An amphibious snake robot that crawls and swims using a central pattern generator," *Color Res. Appl.* **27**(2), 130–135 (2006).
[2] H.T. Lin, G. G. Leisk, and B. Trimmer, "GoQBot: A caterpillar-inspired softbodied rolling robot," *Bioinspir. Biomim.* **6**(2), 026007 (2011).
[3] R. F. Shepherd, A. A. Stokes, J. Freake, et al., "Using explosions to power a soft robot," *Angew. Chem. Int. Ed.* **52**(10), 2892–2896 (2013).
[4] B. Mazzolai, L. Margheri, M. Cianchetti, et al., "Soft-robotic arm inspired by the octopus: II. From artificial requirements to innovative technological solutions," *Bioinspir. Biomim*. **7**(2), 025005 (2012).
[5] T. Zheng, et al., "Model validation of an octopus inspired continuum robotic arm for use in underwater environments," *J. Mech. Robot.* **5**(2), 021004(2013).
[6] S. Seok, et al., "Peristaltic Locomotion with Antagonistic Actuators in Soft Robotics," In: *IEEE International Conference on Robotics & Automation* (IEEE, 2010).
[7] Y. Fei, and W. Pang, "Analysis on nonlinear turning motion of multi-spherical soft robots," *Nonlinear Dyn.* **88**(2), 883–892 (2017).
[8] Q. Pei, et al., "Multiple-degrees-of-freedom electroelastomer roll actuators," *Smart Mater. Struct.* **13**(5), N86 (2004).
[9] R. K. Katzschmann, A. D. Marchese, and D. Rus, "Hydraulic Autonomous Soft Robotic Fish for 3D Swimming," International Symposium on Experimental Robotics, 2016.
[10] H. J. Kim, S. H. Song, and S. H. Ahn, "A turtle-like swimming robot using a smart soft composite (SSC) structure", *Smart Mater. Struct.* **22**(1), 014007 (2012).
[11] J. J. Hubbard, M. Fleming, V. Palmre, et al., "Monolithic IPMC fins for propulsion and maneuvering in bioinspired underwater robotics," *IEEE J. Ocean. Eng*. **39**(3), 540–551 (2014).
[12] S. Nakamaru, S. Maeda, Y. Hara, et al., "Development of Novel Selfoscillating Gel Actuator for Achievement of Chemical Robot," In: *IEEE/RSJ International Conference on Intelligent Robots and Systems, IROS 2009* (IEEE, 2009) pp. 4319–4324.
[13] W. Pang, Y. Fei, and W. He, "Study on Motion Process of Modular Soft Robot," In: *International Conference on Machine Learning and Cybernetics* (IEEE, 2017) pp. 146–151.
[14] S. Seok, et al., "Meshworm: A peristaltic soft robot with antagonistic nickel titanium coil actuators," *IEEE/ASME Trans. Mechatron.* **18**(5), 1485–1497 (2013).
[15] T. E. Jenkins, E. M. Chapman, and M. Bryant, "Bio-inspired online variable recruitment control of fluidic artificial muscles," *Smart Mater. Struct*. **25**(12), 125016 (2016).
[16] R. F. Shepherd, F. Ilievski, W. Choi, et al., "Multigait soft robot," *Proc. Nat. Acad. Sci.* **108**(51), 20400–20403 (2011).
[17] W. Wang, et al., "Locomotion of inchworm-inspired robot made of smart soft composite (SSC)," *Bioinspir. Biomim.* **9**(4), 046006 (2014).
[18] Y. U. Naigong, et al., "Optical flow based mobile robot obstacle avoidance method in unstructured environment," J. Beijing Univ. Technol. (2017).
[19] A. Nasrinahar, and J. H. Chuah, "Intelligent motion planning of a mobile robot with dynamic obstacle avoidance," *J. Veh. Rout. Algor.* **1**, 1–16 (2018).
[20] L. Zong, et al., "Obstacle avoidance handling and mixed integer predictive control for space robots," *Advances in Space Research* **61**(8), S027311771830070X (2018).

https://doi.org/10.1017/S0263574721001867 Published online by Cambridge University Press

[21] Y. Fei and X. Wang, "Study on nonlinear obstacle avoidance on modular soft robots," *Nonlinear Dyn.* **82**(1–2), 891–898 (2015).
[22] T. Wang, et al. "Electrostatic layer jamming variable stiffness for soft robotics," *IEEE/ASME Trans. Mechatron*. **24**(2), 424–433 (2019).
[23] A. Mohammadi Nasab, et al., "A soft gripper with rigidity tunable elastomer strips as ligaments," *Soft Robot.* **4**(4), 411–420 (2017).
[24] M. E. Giannaccini, et al., "Novel design of a soft lightweight pneumatic continuum robot arm with decoupled variable stiffness and positioning," *Soft Robot.* **5**(1), 54–70 (2018).
[25] L. A. Abeach, et al., "A variable stiffness soft gripper using granular jamming and biologically, inspired pneumatic muscles," *J. Bionic Eng.* **2**, 236–246 (2018).
[26] T. Ranzani, et al., "A bioinspired soft manipulator for minimally invasive surgery," *Bioinspir. Biomim.* **10**(3), 035008 (2015).
[27] Y. Wei, et al. "A soft robotic spine with tunable stiffness based on integrated ball joint and particle jamming," *Mechatronics* **33**, 84–92 (2016).
[28] Sadati, Sm Hadi, et al. "Stiffness control of soft robotic manipulator for minimally invasive surgery (mis) using scale jamming." International Conference on Intelligent Robotics and Applications Springer, Cham, 2015.
[29] Li, Yingtian, et al. "Passive Particle Jamming and Its Stiffening of Soft Robotic Grippers." IEEE Transactions on Robotics 33.2(2017):446–455.
[30] P. Wu, W. Jiangbei, and F. Yanqiong, "The structure, design, and closed-loop motion control of a differential drive soft robot," *Soft Robot.* **5**(1), 71 (2018).
[31] H. Jianlong, X. Guangjuan, and L. Zhengwei, "Finite element analysis of super-elastic rubber materials based on the Mooney-Rivlin and Yeoh model," *China Rubber/Plastics Technol. Equip.* (2008).
[32] O. H. Yeoh, "Some forms of the strain energy function for rubber," *Rubber Chem. Technol.* **66**(5), 754–771 (2012).

Cite this article: Z. Liu, Y. Wang, J. Wang, Y. Fei and Q. Du (2022). "An obstacle-avoiding and stiffness-tunable modular bionic soft robot", Robotica **40**, 2651–2665. https://doi.org/10.1017/S0263574721001867

https://doi.org/10.1017/S0263574721001867 Published online by Cambridge University Press